Unsteady transitional swirling flow in the presence of a moving free surface

Roland Bouffanais[1,a)] and David Lo Jacono[2,b)]
[1]*Department of Mechanical Engineering, Massachusetts Institute of Technology, 77 Massachusetts Avenue, Bldg. 5-326, Cambridge, Massachusetts 02139, USA*
[2]*Department of Mechanical and Aerospace Engineering, Monash University, Victoria, 3800 Melbourne, Australia*

(Received 26 February 2009; accepted 21 May 2009; published online 25 June 2009)

Unsteady incompressible viscous flows of a fluid partly enclosed in a cylindrical container with an open top surface are presented in this article. These moving free-surface flows are generated by the steady rotation of the solid bottom end wall. Such type of flows belongs to a group of recirculating lid-driven cavity flows with geometrical axisymmetry. The top surface of the cylindrical cavity is left open so that the free surface can freely deform. The Reynolds regime corresponds to unsteady transitional flows with some incursions in the fully laminar regime. The approach taken here revealed new nonaxisymmetric flow states that are investigated based on a fully three-dimensional solution of the Navier–Stokes equations for the free-surface cylindrical swirling flow without resorting to any symmetry property unlike all other results available in the literature. The results are compared with those of Bouffanais and Lo Jacono ["Transitional cylindrical swirling flow in presence of a flat free surface," Comput. Fluids **38**, 1651 (2009)] corresponding to the exact same parameters but with a flat-and-fixed top free surface. These solutions are obtained through direct numerical simulations based on a highly accurate Legendre spectral element method combined with a moving-grid technique. © *2009 American Institute of Physics*. [DOI: 10.1063/1.3156010]

I. INTRODUCTION

Lid-driven cavity flows present similar features typical of shear-driven recirculating flows such as intense wall jets and shear layers in the vicinity of the driven wall and secondary recirculating flows, which are very dependent on the flow parameters. Nevertheless, the geometry—cubical on one hand and cylindrical on the other hand—dramatically influences the nature and structure of these secondary flows: corner eddies for the cubical cavity and recirculation bubbles in the cylindrical case. Following the pioneering work of Bogatyrev and Gorin[5] and Koseff and Street,[26,27] it was shown that contrary to intuition, the lid-driven cubical cavity flow is essentially three dimensional (3D), even when considering large aspect ratio. It is only recently that the three dimensionality of the lid-driven cylindrical cavity flow was confirmed numerically by Blackburn and Lopez[2,3] after it was suggested but not fully proved experimentally by Sørensen,[44] Spohn *et al.*,[48] Sotiropoulos and Ventikos,[45] and Pereira and Sousa.[38] In 2001, Sotiropoulos and Ventikos[46] gave full experimental evidence of the 3D character of the flow with the onset of nonaxisymmetric modes. The 3D nature of these driven cavity flows is therefore a general characteristic of internal recirculating shear-driven flows.

In the present study, we only consider the cylindrical lid-driven cavity flow also referred to as "swirling" flow without any additional precision. The first experiments by Vogel[52] and later Ronnenberg[41] showed that Ekman suction and pumping, induced by the Ekman layers on the rotating and stationary disks, lead to the formation of a concentrated vortex core along the axis in the closed-cavity case. The two dimensionless groups characterizing this flow are the height-to-radius aspect ratio $\Lambda = H/R$ and the Reynolds number $\mathrm{Re} = R^2\Omega/\nu$, where H and R are, respectively, the height and radius of the cylinder, Ω is the constant angular velocity of the bottom end wall, and ν is the kinematic viscosity of the Newtonian fluid. For specific values of the aspect ratio Λ and above a critical Reynolds number, the vortex core breaks down in the form of one or more recirculation bubbles which are on axis in the closed-cavity case and on or off axis in the open cavity one. Owing to the enormous extent of work in the area of vortex breakdown (VB) (see reviews by Hall,[19] Leibovich,[28] Shtern and Hussain,[43] Kerswell,[25] and Arnt[1]), we refer the reader to the previous reviews for a recall of the central features of VB.

The first comprehensive experimental study of the closed cylindrical container case was undertaken by Escudier[15] and Escudier and Keller,[17] who extended the earlier results of Vogel[52] and Ronnenberg[41] to obtain the first map of VB transitions with respect to the aspect ratio Λ and the Reynolds number. Escudier[15] revealed flow states with one, two, or even three successive breakdowns, as well as a transition from steadiness to unsteadiness. Sørensen[44] extended to a broader range of Reynolds number in the same experiment as Escudier[15] for the closed container and inferred that above a critical Reynolds number in the unsteady flow regime, the meridional flow becomes highly asymmetric. The first experimental study of the open cylindrical container case with a free surface on the top was undertaken by Spohn *et al.*,[47] who highlighted the significant change in the structure and the occurrence and the location of the breakdown bubbles. In the steady closed cylinder case, Hourigan

[a)]Electronic mail: bouffana@mit.edu.
[b)]Electronic mail: david.lojacono@eng.monash.edu.au.

et al.[21] investigated the asymmetric spiraling effects along the cylinder axis prior to the first VB. They argued that the observed asymmetry was purely an experimental artifact and not an evidence of the 3D nature of the flow. Spohn *et al.*[48] were the first to investigate experimentally the origin of possible asymmetric features of the instabilities at their onset. The steady breakdown bubbles reported by Spohn *et al.*[48] showcase asymmetric features comparable to earlier measurements and also to unsteady bubbles observed in circular diffusers by Faler and Leibovich.[18] As a matter of fact, the work of Spohn *et al.*[48] is really a pioneering work in the acceptance of the axisymmetry breaking among fluid experimentalists. It is noteworthy at this point that the complex physics associated with these intricate phenomena occurring in closed/open rotating cylindrical container is still not clearly understood. Recently, Brøns *et al.*[10] elegantly showed how flow visualizations are inherently unable to characterize perfectly axisymmetric VB bubbles. It should be added that while it is no surprise that the flow can be asymmetric in the unsteady case, it is more surprising when it happens in a steady configuration with symmetric boundary conditions. Such states were apparently observed experimentally by Spohn *et al.*[48] and computationally by Sotiropoulos *et al.*[45,46] Brøns *et al.*[9] showed that these asymmetries may be attributed to minute imperfections in the setup, and hence is not a basic fluid mechanical instability.

Apart from the canonical case with a single driving lid in rotation at a constant angular velocity, different variations of the problem have been extensively studied in the past years: e.g., cylinder with co- and counter-rotating end covers by Brøns *et al.*,[11] steady axisymmetric flow in an open cylindrical container with a partially rotating bottom wall by Piva and Meiburg,[39] vortex scenario and bubble generation in a cylindrical cavity with rotating top and bottom by Okulov *et al.*,[37] and swirling flow of a viscoelastic fluid by Escudier and Cullen,[16] Day *et al.*,[13] Xue *et al.*,[53] and Stokes *et al.*[49,50] Mullin *et al.*[35] also included a rod at the axis to control the breakdown, and Pereira and Sousa[38] significantly changed the configuration by replacing the flat rotating bottom cover by a cone. As noted by Brøns *et al.*,[12] all these studies show a large set of flow structures which are quite sensitive to variations of external parameters. Mununga *et al.*[36] and Lo Jacono *et al.*[29] investigated different strategies for the control of VB.

The focus in the present article is on the canonical problem of a cylinder with a rotating bottom end wall but replacing the stationary solid top end wall by a freely moving surface. As mentioned earlier, the flow associated with this problem was first studied experimentally by Spohn *et al.*[47,48] They observed the influence of the top free surface—assuredly clean of surfactants—on the onset, structure, nature, and number of recirculating bubbles. Their central observations are that breakdown bubbles still appear but are off axis and may be attached to the free surface depending on the aspect ratio Λ and the Reynolds number. Of course, such structures could not be observed in the closed-cavity case because of the no-slip condition imposed on the top wall. All the past simulations of free-surface swirling flows rely on the central assumptions that the free surface is flat and clean, which means that the Froude number is taken equal to zero and that surface tension effects are neglected. With these assumptions, the flow is identical to the flow in the lower half part of a cylinder with two solid covers in corotation, i.e., rotating at the same angular velocity. Brøns *et al.*[12] reported a wide range of topologies of VB bubbles in a bottom-driven cylinder with a free surface. Valentine and Jahnke[51] observed in their simulations the existence of one or two toroidal-like types of recirculation bubble having their stagnation lines attached to the free surface depending on the value of the Reynolds number. Their study was complemented by the works of Lopez[30] for oscillating unsteady flows and of Bouffanais and Lo Jacono[8] for unsteady flows at higher Reynolds numbers. Information relevant to the present problem with a free surface all indicate consistent flow behavior at small aspect ratio, i.e., $0.5 \leq \Lambda \leq 1.0$, in that stagnation occurs off axis and associated secondary flow creates a toroidal recirculation bubble. Steady free-surface flows have been computed by Iwatsu[22,23] providing flow state classifications with new flow patterns not revealed in the previous studies.

Gas-liquid interfaces are often modeled as flat, fixed, and stress-free surfaces. This idealization is commonly used by fluid dynamicists performing numerical simulations. Indeed, by resorting to this assumption the physical problem is significantly simplified and thus standard solution techniques can be used to deliver the flow fields. However, this idealization is never realized physically, even in well-controlled experimental setups, and this is mainly because of the presence of small amounts of surfactants. In addition, even for small angular velocities of the bottom end wall, i.e., for small Reynolds numbers, limited deformations of the top surface are always present. These deformations are very often difficult to access by any of the measurement techniques available in laboratory experiments. Compared with swirling flows in a closed cylinder, the VB phenomena occur in different conditions for an open cylinder flow: lower critical Reynolds number, smaller lower-limit aspect ratio Λ at which VB occurs, large size of breakdown bubbles, possible attachment to the top free surface, etc. Moreover, for the relatively "shallow" system corresponding to $\Lambda = 1$, the loss of axisymmetry of these free-surface swirling flows is due to unstable azimuthal modes developing at the interface between the "inner" fluid in quasi-solid-body rotation and the "outer" fluid, where a surface jet of angular momentum exists and is directed toward the cylinder axis.

The present study is mainly motivated by the need to gain insight into the influence of an unsteady and nonflat free surface onto the cylindrical swirling flow. It is important to note that even if the deformation amplitude of the free surface is limited compared to the cylinder height, the relative deformation amplitude may have rapid variations along radial lines. Those rapid variations could potentially have an impact on the various physical terms appearing in the governing Navier–Stokes equations. Ultimately, the reported effects of the relative deformations of the free surface on the physical terms—nonlinear convective terms, pressure gradient, viscous stress—may be extrapolated to cases where the amplitude of the surface deformations is more important.

Lower-Reynolds-number cases display a steady flow behavior which persists in the presence of a free surface, which acquires a steady shape. In addition, for the unsteady case ($\Lambda=1$, $\mathrm{Re}=6000$) studied herein, the free surface displays an unsteady evolution.

To date, all prior attempts to simulate this free-surface flow were limited to the fixed and flat free-surface case and primarily to steady open swirling flows. Such lack of study in the scientific literature of this unsteady open swirling flow with a moving free surface can be understood when reading the following statement from Sarpkaya in his review entitled "Vorticity, free surface and surfactants:"[42] "…the modeling of free-surface phenomena still poses difficulties, not only because of an insufficient understanding of the physics of the vorticity/free-surface interaction, but also because of the necessity to devise and use mathematical formulations, numerical schemes, and physical-property experiments of far greater complexity than had hitherto been used…." Indeed, when considering a real moving free surface, the complexity of the physical problem is dramatically increased. On top of the nonlinearity associated with the Navier–Stokes equations themselves, here we deal with a complicated geometry, which is changes in time and which is part of the solution itself. In addition, the nature of the boundary conditions on the free surface makes their imposition much more difficult compared to standard no-slip or free-slip boundary conditions. This particular point explains why all past studies of this flow problem prior to the one reported in this article used symmetry properties combined with a double-sized computational domain to enforce the stress-free condition at the flat free surface. This accumulation of difficulties calls for elaborate algorithms and numerical techniques.

The mathematical model and the problem formulation are detailed in Sec. II, while the original computational approach of this study is presented in Sec. III. Subsequently, Sec. IV contains all the numerical results corresponding to various physical situations and flow states. Finally, the article ends with Sec. V providing summary and conclusions on the present work.

II. MATHEMATICAL MODEL AND PROBLEM FORMULATION

A. Mathematical description of the problem

The fluid enclosed in the cylindrical cavity is assumed to be incompressible and Newtonian with uniform density and temperature. In the arbitrary Lagrangian–Eulerian (ALE) kinematics,[14] the flow is governed by the modified Navier–Stokes equations

$$\frac{\partial u_i}{\partial t} + (u_j - w_j)\frac{\partial u_i}{\partial x_j} = \frac{\partial \sigma_{ij}^*}{\partial x_j} + g_i, \tag{1}$$

$$\frac{\partial u_j}{\partial x_j} = 0, \tag{2}$$

where $\sigma_{ij}^* = -p\delta_{ij} + 2\nu D_{ij}$ is the reduced Cauchy stress tensor of the fluid, p the static or reduced pressure, D_{ij} the rate-of-deformation tensor, ν the assuredly constant and uniform kinematic viscosity, g_i the components of the acceleration of gravity ($g_1=g_2=0$ and $g_3=-g$), and w_i the components of the ALE mesh velocity. The reader is referred to Ref. 4 for a comprehensive introduction to the ALE kinematics and for the definition of the ALE mesh velocity $\mathbf{w}$. For the sake of clarity, we briefly present here the central details of the mathematical description of this problem in the ALE framework. Inside the fluid domain denoted by $\mathcal{V}$, no-slip boundary conditions are imposed on all cavity walls: the tubular side wall and the steadily rotating bottom end wall. A sketch of the fluid domain along with additional information is depicted in Fig. 1. The mathematical expressions of the no-slip condition on the tubular side wall now account for the varying fluid height and read

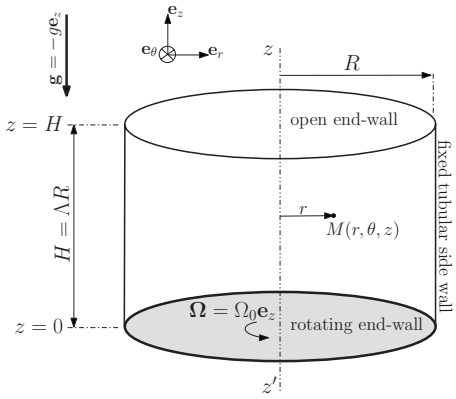

FIG. 1. Sketch of the 3D geometry of the cylindrical cavity.

$$u(r=R,\theta,z,t) = v(r=R,\theta,z,t) = w(r=R,\theta,z,t) = 0,$$
$$0 \le \theta \le 2\pi, \quad 0 \le z \le H + \eta(R,\theta,t), \tag{3}$$

where $\eta(r,\theta,t)$ is the algebraic free-surface elevation at the point of polar coordinates (r,θ) and measured from its equilibrium position $z=H$. The flow is driven by imposing a regularized and steady angular velocity profile to the bottom end wall, which transfers its kinetic energy to the fluid above through shear stresses. The details regarding the imposition of this Dirichlet boundary condition for the velocity field at the spinning disk are discussed in Sec. II B. The top surface is left open and is modeled as a moving and yet clean free surface—i.e., surface tension effects are neglected. The imposition of the dynamic and kinematic boundary conditions (KBCs) at the free surface is discussed in Sec. II C.

B. Angular velocity distribution

Imposing a constant angular velocity profile leads to a singularity (discontinuous behavior in the velocity boundary conditions) at the circular edge between the bottom end wall and the tubular side wall, see Fig. 1. Without adequate treatment, this discontinuous behavior undermines the convergence and the accuracy of any numerical method in the vicinity of the lid. The same remedy as in the lid-driven cubical cavity problem treated by Bouffanais *et al.*[7] is used here for the same reasons and with analogous justifications. A regularized angular velocity profile is employed by pre-

scribing the following high-order polynomial expansion which vanishes along with its first derivatives on the circular edge,

$$\mathbf{\Omega}(r,\theta,z=0,t)=\Omega_0\left[1-\left(\frac{r}{R}\right)^{16}\right]^2\mathbf{e}_z$$

and

$$\mathbf{u}(x,y,z=0,t)=\Omega_0[1-(\sqrt{x^2+y^2}/R)^{16}]^2(x\mathbf{e}_y-y\mathbf{e}_x), \quad (4)$$

for the prescribed velocity field on the bottom end wall in Cartesian coordinates. This profile flattens very quickly near the circular edge $(r/R=1,\theta,z/H=0)$ while away from it, it grows rapidly to a constant value Ω_0 of the angular velocity over a short distance. The highest polynomial order of this distribution is 32. Such high-order polynomial expansion leads to steep velocity gradients in the vicinity of the circular edge of the bottom end wall. This constraint in the grid design has been accounted for in order to ensure the proper resolution of the lid velocity distribution by the spectral element decomposition, see Sec. III.

C. Free-surface modeling

The mathematical problem corresponding to Eqs. (1) and (2) requires the definition of three independent nondimensional parameters to determine completely the flow state. These three parameters are the height-to-radius aspect ratio $\Lambda=H/R$, the Reynolds number $\mathrm{Re}=R^2\Omega_0/\nu$, and the Froude number $\mathrm{Fr}=R^2\Omega_0^2/(gH)=R\Omega_0^2/(g\Lambda)$ based on the maximal prescribed angular velocity Ω_0 of the bottom end wall and the acceleration of gravity g. Based on this set of nondimensional parameters, the governing equations and boundary conditions for this problem can easily be nondimensionalized. The reader is referred to the monograph by Pozrikidis[40] for a detailed discussion of the possible scalings of the Navier–Stokes equations when the sole body force acting is the one due to the gravity. Given our focus here on transitional flows for which Reynolds numbers can be quite high, the choice of scaling is straightforward. It leads to nondimensional governing equations and boundary conditions obtained from the dimensional ones by simply and respectively exchanging ν with 1/Re and g with 1/Fr, see Ref. 40. Furthermore, a comprehensive discussion of the different steps from the dimensionalized governing equations and boundary conditions to the discretized ones can be found in Ref. 4.

It is sometimes convenient to introduce an additional nondimensional number: the Wehausen number denoted as Wh and defined as the ratio between Re and $\mathrm{Fr}^{1/2}$,

$$\mathrm{Wh}=\frac{\mathrm{Re}}{\sqrt{\mathrm{Fr}}}=R^{3/2}\frac{\sqrt{g\Lambda}}{\nu}. \quad (5)$$

This nondimensional number is obviously dependent on the three other nondimensional numbers and may be regarded as a measure of the relative magnitudes of the macroscopic time scales and of the microscopic and viscous diffusive ones. The interest for the Wehausen number lies in the fact that for a given fluid—i.e., for a given kinematic viscosity ν—under the effect of gravitational forces, Wh solely depends on the problem length scale—here the cylinder radius R, the dependence on the aspect ratio Λ being marginal. The Wehausen number has been introduced in the past for the study of large-scale free-surface flows (see Ref. 33) to justify the use of an irrotational flow hypothesis away from the free surface. These arguments correspond to typical free-surface flows encountered in ocean engineering. In the present case, the length scales correspond to typical experimental setup and are therefore clearly smaller. Using $g=9.81$ m s^{-2} and the kinematic viscosity of tap water at ambient temperature $\nu=10^{-6}$ m^2 s^{-1}, one can evaluate the order of the Wehausen number for the cylinder used in a typical experimental setup, of radius $R=H=O(10^{-1})$ m: $\mathrm{Wh}=O(10^5)$. Such a high order for Wh is a further justification of the flat-and-fixed free-surface modeling approach approximation systematically used in the framework of this problem. However, this estimate loses some of its interest when considering the dynamics of some local effects at the free surface highlighted in the present study. Indeed, as mentioned earlier, Wh does not depend on any characteristic velocity scale but solely on the characteristic length scale of the problem. The thorough study of the unsteady flat-and-fixed free-surface problem by Bouffanais and Lo Jacono[8] has revealed some small-scale structures near the free surface. These small-scale structures lead to significantly smaller values of the Wehausen number and this independently of their characteristic velocity or vorticity scales.

The hypothesis of flat-and-fixed free surface is equivalent to imposing a zero-Froude-number condition, which in turn leads to a simplified KBC $w=u_z=0$ at the free surface $z=H$. The KBC expresses the fact that the free surface is a nonpermeable material surface. In the ALE framework, the KBC at the free surface in its most general form reads

$$\mathbf{u}\cdot\hat{\mathbf{n}}=\mathbf{w}\cdot\hat{\mathbf{n}}, \quad (6)$$

where $\hat{\mathbf{n}}$ represents the local unit outward normal vector to the free surface. The scalar equation (6) only constrains the normal component of the mesh velocity $\mathbf{w}$. Some freedom remains for the choice of the values of the tangential part of $\mathbf{w}$. To simplify the implementation, a pure Lagrangian description of the free surface is chosen by imposing the tangential part of $\mathbf{w}$ to be identical to the corresponding one for the fluid velocity. Thus, the KBC takes the very simple form of the following vector equation:

$$\mathbf{u}=\mathbf{w}, \quad (7)$$

at the free surface.

The pressure and velocity boundary conditions at the free surface are both formulated from the dynamic constraint of continuity of normal momentum flux across the free surface while assuming negligible momentum on the air side and neglecting surface tension effects—hypothesis of clean surface without any surfactant. This dynamic boundary condition (DBC) reads

$$\sigma_{ij}^{*}\hat{n}_j=-p\,\delta_{ij}\hat{n}_j+2\nu D_{ij}\hat{n}_j=0 \quad (8)$$

for zero atmospheric pressure. Unlike in the flat-and-fixed free-surface case,[8] the DBC equation (8) does not simplify further but leads to a vanishing integral surface term (denoted by $\mathcal{H}^{\sigma}$ in Ref. 4) into the weak ALE formulation of the

problem—see Ref. 4 for a complete theoretical presentation of this aspect. As emphasized in this last reference, this homogeneous DBC is automatically incorporated into the complete weak formulation of the problem expressed in its strong form by Eqs. (1) and (2). This automatic imposition of the DBC through the weak formulation of the problem is one of the most attractive feature of the newly developed numerical method used in the direct numerical simulation (DNS) of this open cylindrical swirling flow. Along the same line, the specific choice of the ALE kinematics allows to automatically account for the KBC through Eq. (6), or equivalently Eq. (7).

D. Mesh velocity problem

When considering this free-surface swirling flow problem tackled in an interface tracking and ALE frame, the free surface is treated in a Lagrangian way, whereas the fixed tubular side wall and the prescribed-in-motion bottom end wall are studied in the Eulerian frame. It is worth noting that the vector expression Eq. (7) of the KBC is mathematically compatible with the no-slip condition on the tubular side wall expressed by Eq. (3) if and only if one imposes the no-slip condition Eq. (3) to the ALE mesh velocity $\mathbf{w}$ at the contact line defined by $(r=R,\theta,z=H+\eta)$. This homogeneous Dirichlet boundary condition for the mesh velocity on the tubular side wall is supplemented by another homogeneous Dirichlet condition on the bottom end wall $z=0$. As a consequence of the choice of kinematics on the fluid domain boundary—Lagrangian and Eulerian but not yet arbitrary—the values of the mesh velocity are prescribed by the boundary conditions given by Eq. (7) and the two homogeneous Dirichlet conditions on the bottom end wall and tubular side wall. The freedom left for the choice of $\mathbf{w}$ lies solely in the values of this field in the internal fluid domain.

The details associated with the underlying moving-grid technique are dealt with by Bodard *et al.*[4] For the sake of clarity, we only briefly recall here the central details of this method. The determination of the mesh velocity $\mathbf{w}$ in the internal fluid domain is the cornerstone of the moving-grid technique developed in the framework of the ALE formulation. The values of the mesh velocity being prescribed on the boundary, the evaluation of $\mathbf{w}$ is obtained as the solution of the following steady Stokes problem:

$$\boldsymbol{\nabla}\cdot\tilde{\boldsymbol{\sigma}}=\boldsymbol{\nabla}\cdot[-\tilde{p}\mathbf{I}+\tilde{\nu}(\boldsymbol{\nabla}\mathbf{w}+\boldsymbol{\nabla}\mathbf{w}^{T})]=\mathbf{0}, \tag{9}$$

$$\boldsymbol{\nabla}\cdot\mathbf{w}=0, \tag{10}$$

where $\tilde{\boldsymbol{\sigma}}$ can be seen as the Cauchy stress tensor of the mesh, with $\tilde{p}$ and $\tilde{\nu}$ being, respectively, the fictitious mesh pressure and the fictitious kinematic viscosity of the mesh, characterizing the viscosity of the mesh in its flowing motion. The reader is referred to Ref. 4 for the multiple explanations of this choice of incompressible flow motion of the mesh. Finally, the update of the position $\mathbf{x}$ of the mesh points is performed by integrating the following equation:

$$\frac{d\mathbf{x}}{dt}=\mathbf{w}. \tag{11}$$

III. COMPUTATIONAL APPROACH

This section is aimed at providing the reader with a brief but nonetheless essential description of the numerical treatment of the equations governing the problem studied by DNSs using an ALE moving-grid technique jointly with the Legendre spectral element method.

A. Space discretization

A classical Galerkin approximation is applied to the set of governing equations expressed in the weak transient ALE form in order to determine the pressure and the fluid velocity. The Galerkin approximation is then discretized by using the spectral element method with the classical staggered $\mathbb{P}_N-\mathbb{P}_{N-2}$ approach to avoid the development of spurious pressure modes.[32] Discontinuous and continuous approximations are taken for the pressure and fluid velocity, respectively. The mesh velocity is discretized using the same polynomial space as the fluid velocity, namely, $\mathbb{P}_N$, based on a Gauss–Lobatto–Legendre (GLL) grid of order N. For the discontinuous approximation of the pressure, a Gauss–Legendre (GL) grid of order $N-2$ is used. Consequently the ALE Navier–Stokes semidiscrete equations reads

$$\frac{d}{dt}(\mathbf{M}\underline{\mathbf{u}})+\mathbf{C}(\underline{\mathbf{u}},\underline{\mathbf{w}})\underline{\mathbf{u}}+\mathbf{A}\underline{\mathbf{u}}+\mathbf{D}^{T}\underline{p}=\underline{\mathbf{F}}, \tag{12}$$

$$-\mathbf{D}\underline{\mathbf{u}}=\mathbf{0}, \tag{13}$$

$\mathbf{M}$ denoting the tensorized mass matrix, $\mathbf{A}$ the tensorized stiffness matrix, $\mathbf{D}^T$ the tensorized discrete gradient operator, $\mathbf{D}$ the tensorized discrete divergence operator, $\mathbf{C}(\underline{\mathbf{u}},\underline{\mathbf{w}})$ the tensorized discrete convective operator depending both on the fluid and mesh velocity, and $\underline{\mathbf{F}}$ the discrete body force which accounts for the macroscopic effects of the acceleration of gravity g. The update of the position $\mathbf{x}$ of the mesh points is performed by integrating the discrete counterpart of Eq. (11),

$$\frac{d\underline{\mathbf{x}}}{dt}=\underline{\mathbf{w}}. \tag{14}$$

The spectral element grid prior to any motion in the ALE framework and used for all simulations is presented in Fig. 2 in the case $\Lambda=1$. This mesh comprises 440 spectral elements distributed into ten cylindrical layers of different heights but all made of the same distribution of 44 spectral elements. In order to resolve the boundary layer along the tubular side wall, the Ekman shear layer above the rotating bottom end wall, and the surface shear layer below the free surface, the spectral elements are unevenly distributed as can be seen in Fig. 2. The choice of polynomial order in the three space directions, defining the inner GLL and GL grids into each spectral element, is based on a convergence analysis reported by Bouffanais and Lo Jacono:[8] the temporal convergence is achieved using a time step small enough to satisfy the Courant–Friedrichs–Lewy condition, while a polynomial order $N=8$ (except for a very laminar case for which $N=7$ suffices) in all three space directions ensures the spatial convergence. The essential Dirichlet boundary conditions—

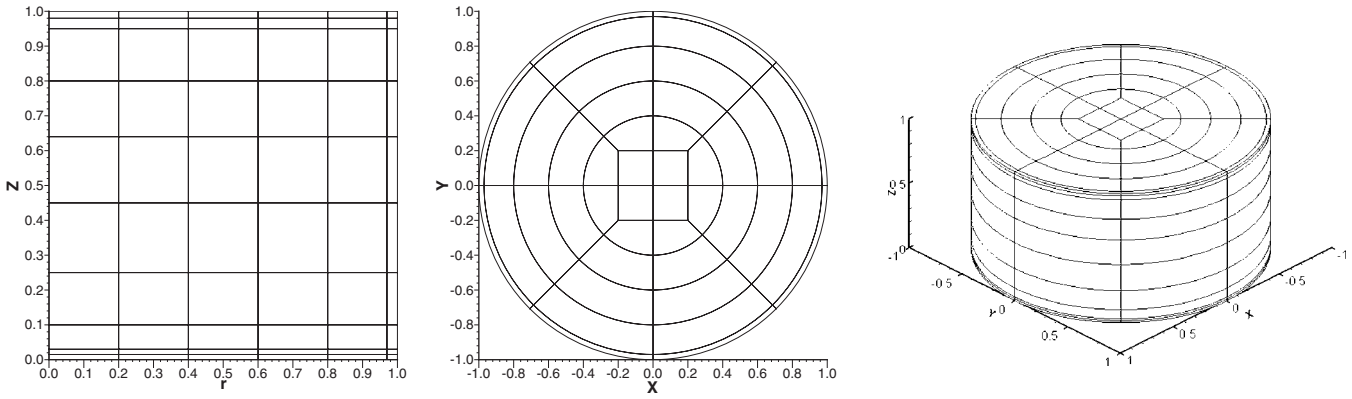

FIG. 2. Left: half-meridional spectral element grid. Center: spectral element grid in any plane normal to the z direction. Right: 3D grid comprising ten cylindrical layers of nonuniform heights made of 44 spectral elements each. Case $\Lambda=1$.

homogeneous for **u** on the tubular side wall as expressed by Eq. (3) and nonhomogeneous for **u** on the rotating bottom end wall as expressed by Eq. (4)—are embodied into the choice of test and trial functions chosen for the velocity field.

B. Time integration

The set of semidiscrete equations (12)–(14) is discretized in time using finite-difference schemes in a decoupled approach. The computation of the linear Helmholtz problem—corresponding to the stiffness matrix **A**—is integrated based on an implicit backward differentiation formula of order 2; the nonlinear convective term—corresponding to the operator **C**—is integrated based on a relatively simple extrapolation method of order 2, introduced by Karniadakis *et al.*[24] The discrete body force vector $\underline{\mathbf{F}}$ appearing in Eq. (12) may be expressed in a more intuitive way as **Mg**, where **M** denotes the tensorized mass matrix. The fully discretized set of governing equations reads

$$\left(\frac{3\mathbf{M}^{n+1}}{2\Delta t}+\mathbf{A}^{n+1}\right)\underline{\mathbf{u}}^{n+1}-(\mathbf{D}^{n+1})^{T}\underline{p}^{n+1}$$
$$=\frac{1}{\Delta t}\left(2\mathbf{M}^{n}\underline{\mathbf{u}}^{n}-\frac{1}{2}\mathbf{M}^{n-1}\underline{\mathbf{u}}^{n-1}\right)+\mathbf{M}^{n+1}\underline{\mathbf{g}}^{n+1}-\mathbf{C}^{n+1}\underline{\mathbf{u}}^{n+1}, \quad (15)$$

$$\mathbf{C}^{n+1}\underline{\mathbf{u}}^{n+1}=2\mathbf{C}^{n}(\underline{\mathbf{u}}^{n},\underline{\mathbf{w}}^{n})\underline{\mathbf{u}}^{n}-\mathbf{C}^{n-1}(\underline{\mathbf{u}}^{n-1},\underline{\mathbf{w}}^{n-1})\underline{\mathbf{u}}^{n-1}, \quad (16)$$

$$-\mathbf{D}^{n+1}\underline{\mathbf{u}}^{n+1}=\underline{0}, \quad (17)$$

$$\underline{\mathbf{x}}^{n+1}=\underline{\mathbf{x}}^{n}+\Delta t\left(\frac{23}{12}\underline{\mathbf{w}}^{n}-\frac{16}{12}\underline{\mathbf{w}}^{n-1}+\frac{5}{12}\underline{\mathbf{w}}^{n-2}\right), \quad (18)$$

where Δt is the time step. Again for this technical aspect, the reader is referred to Ref. 4.

C. Computational parameters

The DNSs correspond to three different values of the Reynolds number sharing the same aspect ratio $\Lambda=1$. As stated earlier, the physics of these free-surface swirling flows depends critically on both the Reynolds number and the height-to-radius aspect ratio Λ. Very often, situations corresponding to extreme values of Λ have been studied, as they generally lead to simplified flow mechanisms. For instance, shallow systems ($\Lambda<1$) are often referred to as "rotor-stator" configurations, in which the fluid is almost in a state of solid-body rotation. On the other hand, deep systems associated with large values of Λ generate recirculation bubbles away from the free surface and generally on the cylinder axis. Consequently, systems corresponding to values of Λ close to unity are intermediate in the sense that the physics of the flow observed is a complex combination of the general features reported for the shallow and deep systems. Given the nondimensionalization used, these three cases correspond to the same Froude number. In terms of initial conditions, the steady rotation is started from the steady state (statistically steady state) reached in the fixed-and-flat free-surface simulations (a) and (b) [(c)] from Ref. 8. The steady (statistically steady) state for cases (a) and (b) [(c)] is reached after a transient of very short duration. The physical and computational parameters corresponding to the three moving cases are reported in Table I.

In this study, the primary focus is on the unsteady case (c). The value of the Reynolds number is intentionally set to a high value compared to previous studies—the highest to our knowledge—in order to ensure producing fields of a relative intensity at the free surface. The central case (c) is supplemented with two secondary cases (a) and (b) allowing to better understand the complex dynamics of the primary case ($\Lambda=1$, Re=6000). The value of the Froude number Fr=0.1 corresponds to a practical configuration in which the value of Ω_0 corresponds to Re=6000, case (c), with $H=R=32.5$ mm as in the experimental setup used by Lo Jacono *et al.*[29] To simplify the comparison between the different

TABLE I. Parameters and characteristics of the cases considered. The time step Δt is expressed in Ω_0^{-1} units and N refers to the same polynomial order used in all space directions.

Case	Re	$\Lambda=H/R$	Fr	Time step Δt	Time evolution	N
(a)	900	1.0	0.1	0.0025	Steady	7
(b)	1500	1.0	0.1	0.0025	Steady	8
(c)	6000	1.0	0.1	0.0010	Unsteady	8

cases, the same value of the Froude number is taken for cases (*a*) and (*b*). In a common approach to unsteady problems, the complex dynamics of case (*c*) is analyzed by means of an averaging process supplemented with instantaneous flow sample. The mean flow is obtained by averaging 400 flow samples corresponding to successive flow states extracted every 0.1 time units (or equivalently ten samples are extracted for each complete turn of the bottom end wall, i.e., every 100 iterations). Subsequently, the root-mean-square (rms) fluctuations of flow fields are calculated using the same extracted flow samples and the mean flow field obtained earlier. Given the moving-grid nature of the present DNS, the averaging process poses severe technical difficulties as the database comprises flow samples being all defined on different grids. In the spectral element framework and given the high-order representation of the flow fields, no simple interpolation procedure can be used to transfer the data onto some sort of common grid. To circumvent this central issue, two procedures have been adopted. First for the free-surface elevation, a one-dimensional line of surface points along a radial line has been extracted and interpolated using a standard quadratic spline interpolation procedure. All the interpolated lines have then been averaged to lead to the average free-surface profile. This procedure has the advantage of being straightforward and global (by opposition to the local nature of the spectral element method) but leads to an oversmoothing of the data. The second procedure concerns the internal flow field and uses a high-order remeshing procedure developed by Bouffanais and Deville[6] to transfer the flow fields from their deformed grid at instant t onto the initial grid at $t=0$ which is shown in Fig. 2 and has a flat free surface. Such procedure has the advantages of being high order and local and has proved to conserve the spectral accuracy,[6] except here close to the free surface because of its flattening. It is important to bear in mind that this "flattening" effect appears only in the postprocessing and averaging procedure, the DNS being carried out with a moving nonflat free surface.

IV. NUMERICAL RESULTS

The present study is primarily intended to shed a new light on the open swirling cylinder problem in unsteady and nonaxisymmetric configurations. Indeed, much attention has been paid to the steady and/or axisymmetric flow states. The experimental studies of deep systems—corresponding to $\Lambda > 1$—performed independently and successively by Young *et al.*,[54] Hirsa *et al.*,[20] and Miraghaie *et al.*[34] revealed that the instability mode is concentrated in the vicinity of the wall jet along the tubular side wall. This wall jet is generated by the rotation of the bottom end wall and is turned upwards by the presence of the tubular side wall. As mentioned by Piva and Meiburg:[39] "this instability mode does not lead to a surface deflection, so that it can be captured in numerical simulations assuming a flat, stress-free surface." Conversely, the instability modes for shallow systems—corresponding to $\Lambda \leq 1$—are concentrated in the interfacial region denoted by Υ in Ref. 8 and where the surface radial jet of angular momentum impinges onto the inner cylindrical core in a state of quasi-solid-body rotation. As it is shown in the sequel, these unstable modes yield free-surface deflection, which becomes nonaxisymmetric at sufficiently large Reynolds number. For those shallow cases, the flat and stress-free modeling of the free surface is no longer an acceptable hypothesis.

For sufficiently small Reynolds number and irrespective of Λ, the basic flow state is stable. As noted by Lopez *et al.*,[31] when Re is increased, the basic flow state loses stability via a variety of Hopf bifurcations. It is worth noting that when Re tends to infinity, the stream surfaces and vortex surfaces—giving the streamlines and vortex lines by intersection with a meridional plane—must coincide. At this point, the presence of a flat free surface poses problem because of the constraint of having orthogonal streamlines and vortex lines on it. This apparent paradox is unraveled by simply letting the free surface move, which is exactly what is done in the present numerical framework. Nevertheless, experiments carried out by Spohn *et al.*[47,48] showed that even at Re=6000 the tangential flow is extremely intense compared to the normal one, leading to small free-surface deformations. It is very likely that these small amplitude deformations are not sufficient to solve our apparent paradox. At low Reynolds number, like those of cases (*a*) and (*b*), the viscosity acts on the velocity field to allow the latter condition of orthogonality to be fulfilled. But when the Reynolds number is increased, the action of viscosity and the limited deformation of the free surface are not sufficient to bring back the orthogonality of the two sets of lines. Therefore, the flow must either lose its axisymmetry or become unsteady in order to allow to drop the orthogonality condition. The experiments by Spohn *et al.*[48] suggest that the open swirling flow first go through the unsteady path.

A. Free-surface profiles

Considering the nonflat free-surface case, it appears natural to primarily focus on the determination of the free-surface elevation η. Figure 3 (left) displays the relative surface elevation η/H in any meridional plane for both steady cases (*a*) and (*b*). 3D views of these two cases are available in Fig. 4. One clearly distinguishes two regions corresponding to surface elevations of opposite signs. In the inner-core region of the flow, say, $r/R \leq 0.4$, the algebraic surface elevation is the largest in absolute value and a large trough forms. This internal trough is surrounded by an outer region of strictly positive surface elevation all the way to the circular contact line along the tubular side wall. The radial position of this ring crest is located around $r/R=0.9$ and its amplitude is much smaller than the one of the trough measured on the cylinder axis. The outer ring of positive η is generated by the impingement of the tubular wall jet, consequence of the pumping effect of the Ekman layer above the rotating disk. The inner trough is itself another consequence of this Ekman layer but through its sucking effect which completes the large meridional circulation generated by the motion of the disk. It also corresponds to the region of the flow in a state of quasi-solid-body rotation. The sharp drop to $\eta/H=0$ observed when approaching the tubular side wall is justified by the absence of dynamics of the contact line between

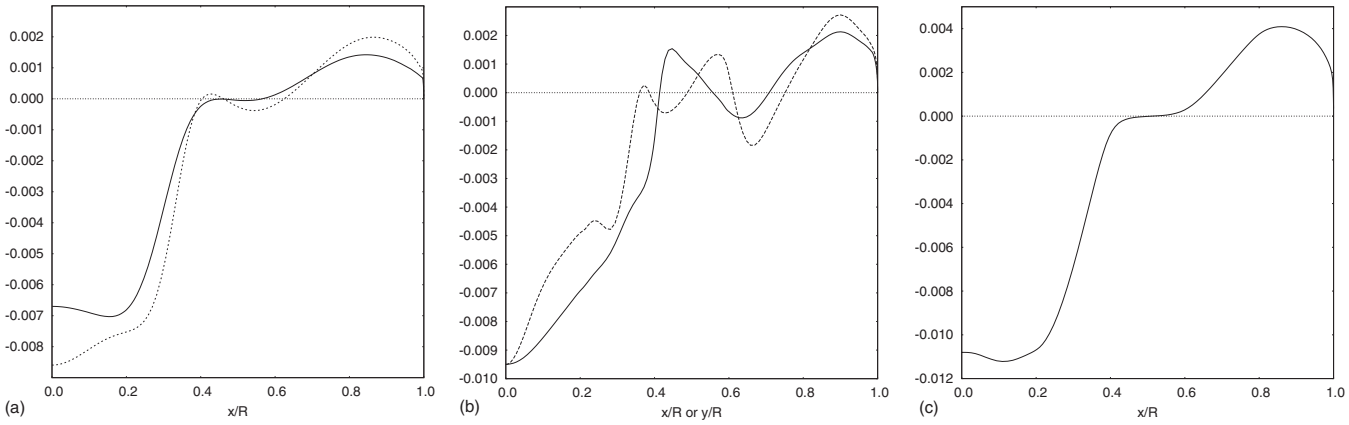

FIG. 3. Relative free-surface elevation η/H measured from the position $z=H$ at rest in a meridional plane. Left: solid line, Re=900; dotted line, Re=1500. Center: Re=6000 (instantaneous flow sample); solid line, meridional plane $y/R=0$; dashed line, meridional plane $x/R=0$. Right: Re=6000 interpolated average.

the three phases: fluid, gas, and solid. Indeed, surface tension is neglected and a no-slip condition is imposed to the fluid on the tubular side wall, while the top surface is free to move, see Sec. II C. Nonetheless, the rapid variations of η/H do not cause any problem given the very high resolution of the mesh near the tubular side wall, see Fig. 2.

As far as the comparison between the cases at Re=900 and Re=1500 is concerned, one may globally note a more pronounced free-surface deformation at higher Re: the deepness of the trough is more important in case (b), and the crest of the outer ring is higher in case (b). On top of those global remarks, three important specific items are to be pointed out. First, one could expect the deepest free-surface point to be located on axis. This is the case at Re=1500 but not at Re =900, where the presence of the on-axis VB bubble limits the sucking effect of the Ekman layer. At Re=1500, the recirculation bubble becomes off-axis and toroidal, which therefore allows for a more important sucking effect along the cylinder axis. The second point is related to the radial location of the maximum of the ring crest: the radius of this maximum appears to be shifted toward the cylinder radius when increasing Re. Bearing in mind that the crest is generated by the tubular wall jet, one may recall that the thickness of this wall jet is reduced with increasing Re, which therefore explains the observed maximum shift of the crest. The third item refers to the transition region between the positive and negative regions of η. This transition region is in relationship with the interfacial zone Υ where the instabilities are concentrated—see Ref. 8: for Re=900 almost no elevation of the free surface is observed, while at Re=1500 an additional small crest is observed followed radially by a second small trough before reaching the largest crest ring.

Based on axisymmetric steady state results, Piva and Meiburg[39] extrapolated the leading order free-surface deflection—denoted by h in their journal article—using the balance of normal stresses at the free surface. In their study, Piva and Meiburg focused on the steady axisymmetric open swirling flow with a partially rotating bottom end wall. It is important to note that their results shown in Fig. 14 of Ref. 39 are only extrapolated results from numerical data obtained using a flat stress-free modeling for the free surface. In their Fig. 14, only the case $D=1$ corresponding to a complete rotation of the bottom wall is of interest to us as it corresponds exactly to our case (a). It appears that their very interesting results for $D=1$ capture roughly the trends and variations. However, they are not able to capture the three important items discussed above.

When increasing the Reynolds number up to Re=6000, the numerical simulation yields a nonaxisymmetric free-surface shape as can be seen in two orthogonal meridional planes in Fig. 3 (center) and in a 3D view in Fig. 4. The interpolated average (see Sec. III C) of the relative free-

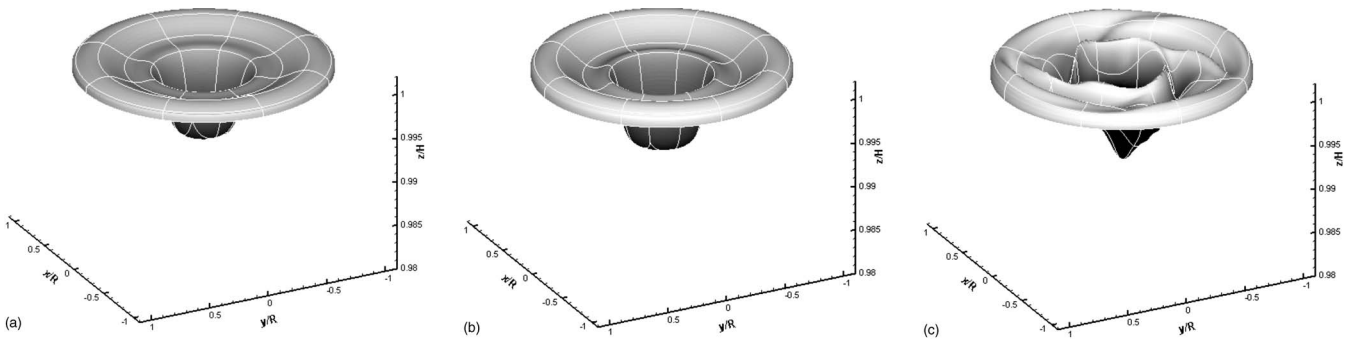

FIG. 4. 3D views of the free-surface shape η/H measured from the position $z=H$ at rest. Left: Re=900; center: Re=1500; right: Re=6000 (instantaneous flow sample). The spectral element grid appears in solid white line to enhance the 3D visualization.

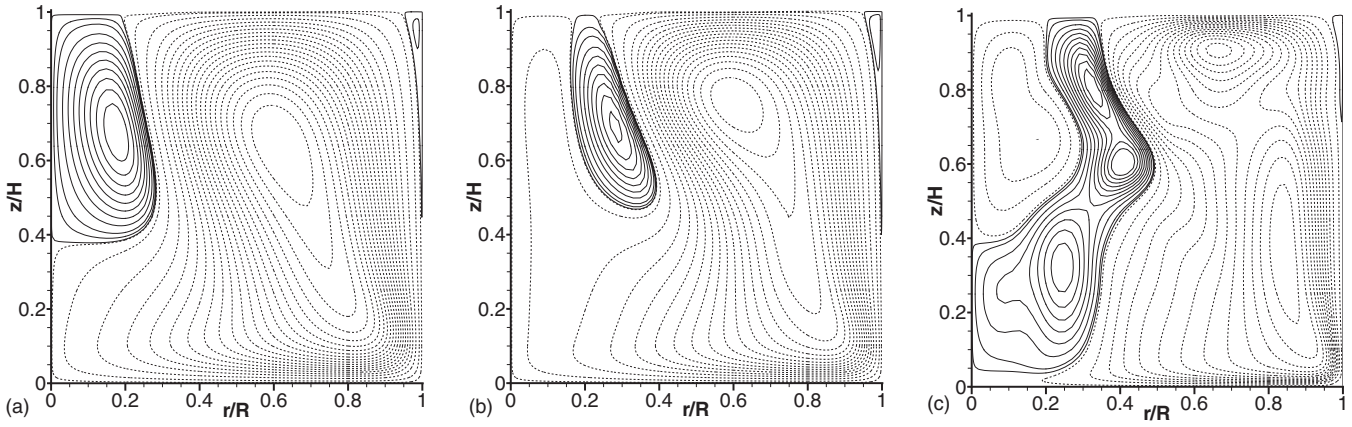

FIG. 5. Contours of streamlines in a meridional plane. Left: Re=900; center: Re=1500; right: Re=6000 (average). The 30 contours are nonuniformly spaced for visualization purposes, 20 equally spaced negative contours and 10 equally spaced positive contours.

surface elevation is shown in Fig. 3 (right). The comments associated with the comparison of cases (*a*) and (*b*) remain valid for this higher-Reynolds-number case. One may, however, note in Fig. 3 the more complex radial variations of η in the larger transition region between the inner trough and the outer crest ring. In the flat free-surface case by Bouffanais and Lo Jacono,[8] the unstable modes were found to be active in this region comprising the interfacial zone Υ. The 3D view in the bottom row of Fig. 4 reveals a free-surface shape of "bathtub sink-vortex" type. Compared to the laminar cases (*a*) and (*b*), the free-surface elevation for the unsteady transitional case at Re=6000 displays extremely rapid variations in space, and hence a less "soft" aspect. In practice, the free surface is never perfectly clean of surfactants, which would inevitably act onto these abrupt spatial variations and lead to a "softer" free-surface shape.

B. Vortex breakdown bubbles and meridional flow fields

We consider now the two steady flows for $\Lambda=1$ and Re=900 and 1500 corresponding to cases (*a*) and (*b*), respectively. Figure 5 (left) displays the streamlines of these flows into any meridional plane. Both of these flows present a large axisymmetric VB bubble attached to the free surface, in agreement with the experimental results from Spohn *et al.*[48] These recirculation zones are characteristic of these swirling flows due to the conjugate effects of the centrifugal force and the overturning flow induced by the presence of the tubular side wall. The central difference between the low-Reynolds-number cases (*a*) and (*b*) is the shape of the recirculation, which becomes toroidal after leaving the axis when the Reynolds number is increased from 900 up to 1 500. For both of these flows, the streamlines are extremely close to those obtained in the flat stress-free model except near the contact line $(r=R,\theta,z=H+\eta)$. A small recirculation bubble appears near this contact line. It is attached to the free surface and stretched from about half-height of the cavity up to the free surface. This VB bubble is related to the crest ring described in Sec. IV A. It is important to note that experimentally this small recirculation bubble may not be present because of unavoidable dynamics of the contact line, which is not accounted for in the present simulations. In addition, the presence of small amounts of surfactants affects the cleanliness of the surface. This notably modifies the contact angle and the free-surface shape near the contact line. The same observation and conclusions apply to the unsteady case (*c*) at Re=6000, for which the streamlines at a given instant are represented in Fig. 5 (right).

In the second step, the contours of the radial, azimuthal, and axial velocity components in any meridional plane are given in Fig. 6. These data are supplemented with the contours of the axial component of the angular momentum $\Gamma=ru_\theta$ still in Fig. 6, extreme right column. Given the small Reynolds numbers in both cases, it is clear that the structures of these fields are extremely close to those obtained using the flat stress-free model. The only notable difference lies in the contours of the axial velocity component u_z. Indeed, the zero-Froude-number condition imposed in the flat free-surface modeling in lieu of the KBC led to a vanishing axial velocity at the free surface. In this study, this condition is relaxed and the real KBC is imposed allowing to have nonzero axial velocity at the free surface. Consequently, we observe now nonzero contours terminating at the free surface, which was impossible previously. The distribution of contours of u_z are to be put together with the surface elevations depicted in Fig. 3. Given the limited surface deflection of the free surface, its local unit normal vector $\hat{\mathbf{n}}$ is everywhere close to the unit vector in the z direction. As the normal component of the fluid velocity is responsible for free-surface deformations, in this case it is u_z that is mainly responsible for the observed surface elevation. One may notice that we recover from the distribution of contours of u_z at the free surface the two regions of positive and negative η.

The previous analysis is further confirmed by the contours of the three velocity components and of the axial angular momentum for an instantaneous flow sample, presented in Fig. 7, in two orthogonal meridional planes. The contours of these four averaged quantities are found to be extremely close to those obtained in the flat-and-fixed free-surface case reported by Bouffanais and Lo Jacono,[8] and hence are not reproduced herein. Even at such high Reynolds number, the presence of a moving free surface does not yield

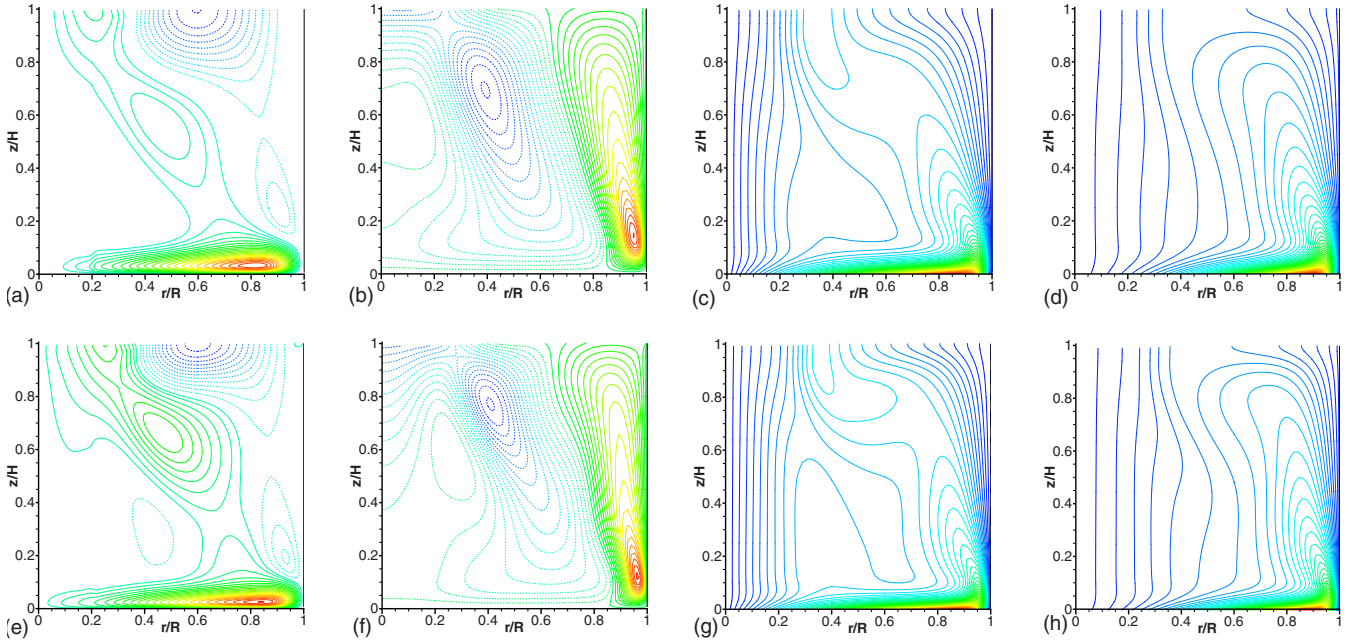

FIG. 6. (Color online) Contours in a meridional plane for the case $\Lambda=1$ with a free surface. Top row: case Re=900; bottom row: case Re=1500. From left column to right column: radial velocity component u_r, axial velocity component $w=u_z$, azimuthal velocity component u_θ, and axial angular momentum component $\Gamma=ru_\theta$. The 35 contours are uniformly spaced between -0.06 and 0.145 for u_r and between -0.09 and 0.12 for u_z. The 50 contours are uniformly spaced between 0 and 1 for u_θ and Γ.

a very different flow dynamics on average. Nonetheless, the instantaneous flow samples display a different set of features with and without a moving free surface.

A careful analysis of the vortex lines for the instantaneous flow sample shows a bending in the whole meridian plane. This bending is very significant in the region $0.4 \leq r/R \leq 0.8$ and $0.4 \leq z/H \leq 1$, which corresponds to the limit between the primary recirculation of the flow and the secondary recirculation bubble. The jetlike shear layer along the tubular side wall is turned into the interior of the flow by the free surface. Focusing on the axial velocity component u_z, the comparison of the respective contours of u_z in Fig. 7 and in the corresponding figure by Bouffanais and Lo Jacono[8] highlights the higher intensity of this shear layer in

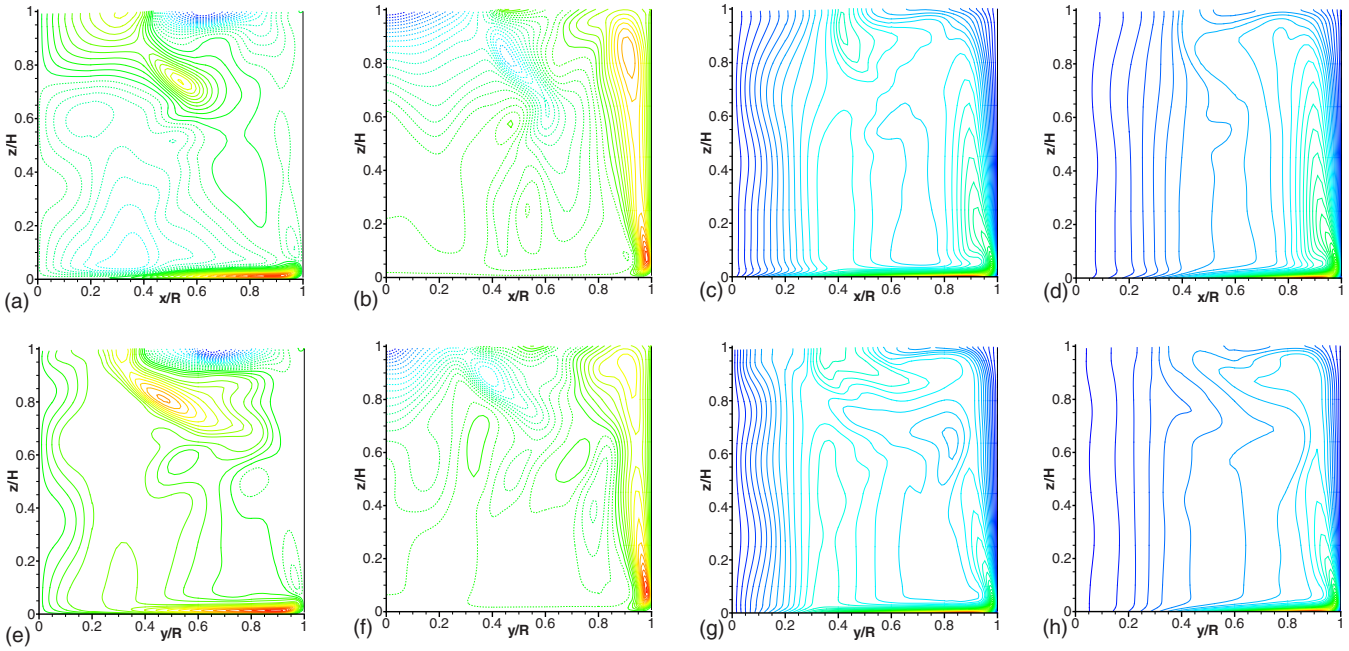

FIG. 7. (Color online) Contours in two orthogonal meridional planes for the case $\Lambda=1$ and Re=6000 with a free surface. Instantaneous flow sample. Top row: meridional plane $y/R=0$; bottom row: meridional plane $x/R=0$. From left column to right column: radial velocity component u_r, axial velocity component u_z, azimuthal velocity component u_θ, and axial angular momentum $\Gamma=ru_\theta$. The 50 contours are uniformly spaced between -0.13 and 0.16 for u_r, between -0.09 and 0.14 for u_z, and between 0 and 1 for u_θ. The 100 contours are uniformly spaced between 0 and 1 for Γ.

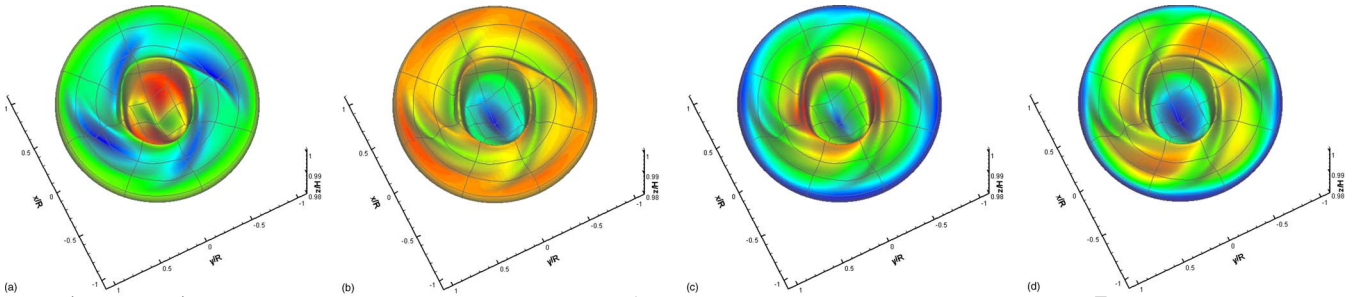

FIG. 8. (Color online) Contours on the free surface $z=H+\eta$ for the case $\Lambda=1$ and Re=6000. From left to right: u_r, u_z, u_θ, and $\Gamma=ru_\theta$. Contour levels are the same as those in Fig. 7. The spectral element grid appears in solid dark-gray line to enhance the 3D visualization.

the moving free-surface case. In the flat case, the axial velocity has monotone decreasing variations in the increasing z direction, while we observe a local maximum of u_z near the position $(r/R=0.9, z/H=0.9)$. The structure of the jetlike shear layer appears therefore modified by the presence of the free surface.

The distribution of contours of u_z at the free surface $z=H+\eta$ again reflects well the calculated free-surface elevation shown in Fig. 3. For instance, the local positive extrema of η at $r/R\simeq 0.5$ and the local negative extrema at $r/R\simeq 0.4$ and $r/R\simeq 0.6$ are well predicted by the variations of u_z at the free surface.

C. Free-surface flow fields

All the previous results dealing with the transitional case (c) reveals a complex flow dynamics due to instabilities developing from a steady stable flow similar to the steady laminar case (b). The study of the rms fluctuations of the flow fields at the free surface presented by Bouffanais and Lo Jacono[8] reveals the existence of an annular region with $0.3\leq r/R\leq 0.4$, where the fluctuations of u_r, u_θ, and Γ are intense. This region was related to the interfacial zone Υ and in the sequel both of these zones will be indifferently denoted by Υ. The statistical analysis of the flow samples corresponding to case (c) allows the study of the rms fluctuations of u_z at the free surface. It is expected to have intense rms fluctuations of u_z in Υ given the very clear and unsteady deformation of the free surface in Fig. 3 for $r/R\simeq 0.4$.

Figure 8 presents the flooded contours of the three cylindrical velocity components and of Γ on the deformed free surface. It is noteworthy to focus our comments onto the axial angular momentum Γ. Four radial jets (two groups of two jets) are visible at the free surface. The two groups of two jets are of different intensity and the most intense one leads to more important surface deflections in the region Υ. This observation can be justified as follows: when the radial free-surface jet of angular momentum impinges on the inner fluid in quasi-solid-body-rotation, the larger part of momentum is redirected downward, while a non-negligible part of it is redirected upward, thereby deforming the free surface.

D. Study of some nonlinear convective terms

Before concluding this study of the moving free-surface swirling flow, we present the variations of some radial and azimuthal nonlinear terms at the free surface. The magnitude of the terms NL rk and NL tk, $k=1,2,3$—see Table II for mathematical expressions—has been calculated along a radial line $(r,\theta=0,z=H+\eta)$ that follows the shape of the free surface. These results are compared to those corresponding to the flat-and-fixed free-surface case reported by Bouffanais and Lo Jacono[8] for cases $(a)-(c)$. Theses radial variations of the terms in Table II are reported in Fig. 9 for cases (a) and (b) and in Fig. 10 for cases (b) and (c). The goal in this section is to highlight the differences in those terms when considering the moving free-surface model as opposed to the flat-and-fixed one, denoted as "FS" and "SF," respectively, in Figs. 9 and 10.

Starting first with the term NL $r1=-u_r\partial u_r/\partial r$, one should observe no substantial change in the variations trend, but for all three Reynolds numbers the FS terms have a reduced magnitude compared to their SF counterparts. The flat-and-fixed free-surface assumption used by Bouffanais and Lo Jacono[8] leads to a systematic overestimation of the radial nonlinear term NL $r1$.

Exactly the same analysis and comments can be made for the radial variations of the centrifugal acceleration NL $r2=u_\theta^2/r$. In addition, the appearance of a local minimum for the centrifugal acceleration in the interfacial zone Υ has been pointed out by Bouffanais and Lo Jacono[8] for case (c). This local minimum is still observable for the FS term NL $r2$, and it is even more pronounced and affects a broader radial interval $0.05\leq r/R\leq 0.45$.

TABLE II. Labels of the different nonlinear terms from the momentum budget equation, similarly to Bouffanais and Lo Jacono (Ref. 8).

Name	Expression
NL $r1$	$-u_r\dfrac{\partial u_r}{\partial r}$
NL $r2$	$+\dfrac{u_\theta^2}{r}$
NL $r3$	$-u_z\dfrac{\partial u_r}{\partial z}$
NL $t1$	$-u_r\dfrac{\partial u_\theta}{\partial r}$
NL $t2$	$-\dfrac{u_r u_\theta}{r}$
NL $t3$	$-u_z\dfrac{\partial u_\theta}{\partial z}$

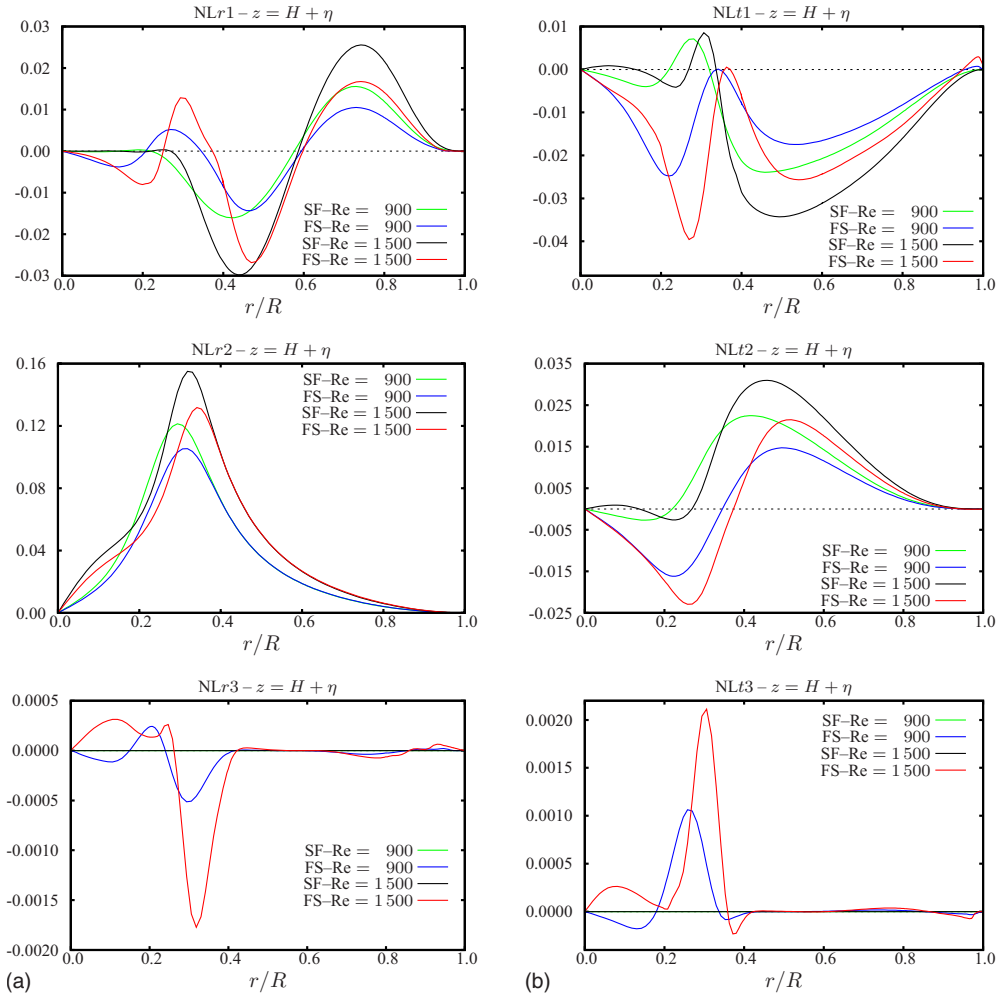

FIG. 9. (Color online) Variations at the free surface of nonlinear terms along a radial line that follows the shape of the free surface. Cases (*a*) and (*b*). Left column: terms NL *rk*, $k=1,2,3$; right column: terms NL *tk*, $k=1,2,3$. SF stands for stress-free and refers to the flat stress-free model and FS stands for free surface. The terminology refers to Table II.

By definition, the nonlinear term NL $r3=-u_z \partial u_r/\partial z$ vanishes at the free surface when considering the flat-and-fixed free-surface hypothesis. For cases (*a*) and (*b*), the magnitude of NL *r*3 is extremely small compared to NL *r*1 and NL *r*2. Consequently, we can conclude to a very limited influence of this term in the flow dynamics, even for case (*c*) at Re $=6000$. The low magnitude of the axial velocity at the free surface seems responsible for this. Again, exactly the same analysis and comments can be made for the azimuthal term NL $t3=-u_z \partial u_\theta/\partial z$.

Contrary to what have been observed for the radial terms NL *r*1 and NL *r*2, the azimuthal terms NL *t*1 and NL *t*2 have their first local minimum in the interval $0.2 \le r/R \le 0.4$, which is underestimated in the flat-and-fixed free-surface framework. For case (*c*) at Re$=6000$, the SF term NL *t*1 shows a local maximum instead of a high-magnitude local minimum found for the FS NL *t*1 term. In addition, the Coriolis term NL *t*2 is globally underestimated in the flat-and-fixed case.

All the results presented in this section confirm some deficiencies of the flat-and-fixed free-surface model when dealing with some nonlinear terms appearing in the governing equations. These deficiencies are obviously more important at the free surface than closer to the rotating disk. Finally, one should point out that the motion of the free surface is shown to be not necessary for the instabilities to grow and for the system to become unsteady and nonaxisymmetric, though it appears to influence these transitions.

V. CONCLUSIONS

The incompressible flow of a viscous fluid enclosed in a cylindrical container with a moving free surface and driven by the constant rotation of the bottom wall has been thoroughly investigated in this article. The top surface of the cylindrical cavity is left open with a clean free surface subject to KBC and DBC. No-slip conditions are imposed on the side wall and on the rotating bottom end wall by means of a regularized angular velocity profile.

New flow states have been investigated based on a fully 3D solution of the Navier–Stokes equations for the free-surface cylindrical swirling flow using a moving-grid technique in the ALE framework. The DBC is automatically incorporated into the complete weak formulation of the problem. This automatic imposition of this DBC through the weak formulation of the problem is one of the most attractive

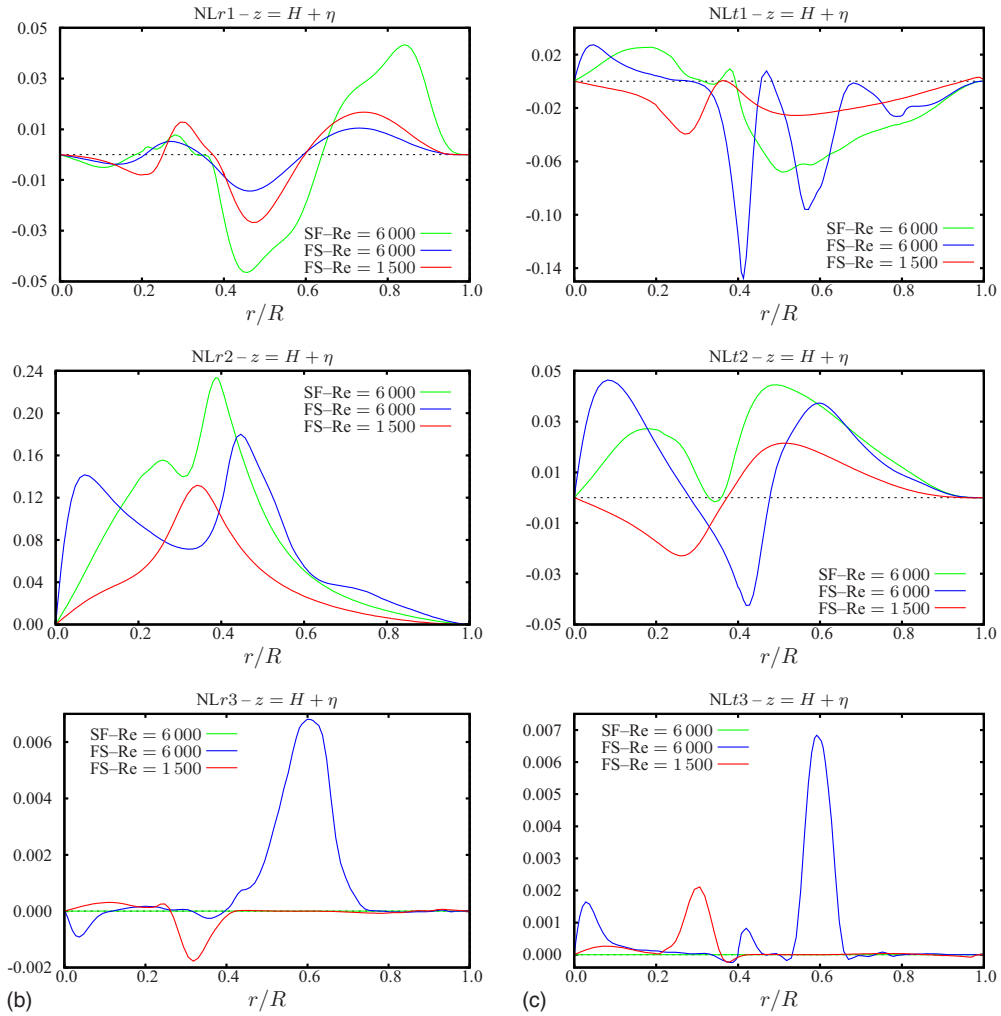

FIG. 10. (Color online) Variations at the free surface of nonlinear terms along a radial line that follows the shape of the free surface. Cases (*b*) and (*c*). Left column: terms NL *rk*, $k=1,2,3$; right column: terms NL *tk*, $k=1,2,3$. SF stands for stress-free and refers to the flat stress-free model and FS stands for free surface. The terminology refers to Table II.

feature of the newly developed numerical method. Along the same line, the specific choice of the ALE kinematics allows to automatically account for the KBC. To our knowledge, the present study delivers the first results for this free-surface swirling flow problem.

Three different cases corresponding to three different values of the Reynolds number have been considered while fixing $\Lambda=1$. The shape of the free surface leads globally to a deep trough around the axis generated by the sucking effect of the Ekman layer above the rotating disk. A small crest ring appears due to the impingement of the tubular wall jet onto the free surface. The location of the VB bubble influences locally the shape of the free surface. At Re=6000, the shape of the free surface loses its axisymmetry and reveals secondary smaller crests and troughs in the interfacial region Υ. For all Re, a smaller recirculation bubble forms near the contact line and the axial velocity component is the most affected by the motion of the free surface. The distribution of axial velocity at the free surface is in good agreement with the free-surface shapes calculated.

For the highest-Reynolds-number case considered (Re =6000), the analysis of the flow at the free surface reveals the presence of two groups of two radial jets of axial angular momentum, which are impinging onto the inner core in quasi-solid-body rotation. On average, the flow dynamics is very similar to the one obtained in the flat-and-fixed free-surface case by Bouffanais and Lo Jacono.[8] However, instantaneous flow samples show distinctive features with and without a flat free surface. The analysis of some nonlinear convective terms central to the flow dynamics confirms the differences when having or not a flat free surface.

ACKNOWLEDGMENTS

The authors would like to thank Professor Michel Deville for fruitful discussions. This research is being partially funded by a Swiss National Science Foundation grant (Grant No. 200020-101707) and Fellowship Nos. PBEL2-112259 and PBELA-118718, whose supports are gratefully

acknowledged. The DNS data were obtained on supercomputing facilities on the Pleiades clusters at EPFL-ISE.

[1] R. E. A. Arndt, "Cavitation in vortical flows," Annu. Rev. Fluid Mech. **34**, 143 (2002).
[2] H. M. Blackburn and J. M. Lopez, "Symmetry breaking of the flow in a cylinder driven by a rotating end wall," Phys. Fluids **12**, 2698 (2000).
[3] H. M. Blackburn and J. M. Lopez, "Modulated rotating waves in an enclosed swirling flow," J. Fluid Mech. **465**, 33 (2002).
[4] N. Bodard, R. Bouffanais, and M. O. Deville, "Solution of moving boundary problems by the spectral element method," Appl. Numer. Math. **58**, 968 (2008).
[5] V. Y. A. Bogatyrev and A. V. Gorin, "End effects in rectangular cavities," Fluid Mech.-Sov. Res. **7**, 101 (1978).
[6] R. Bouffanais and M. O. Deville, "Mesh update techniques for free-surface flow solvers using spectral element method," J. Sci. Comput. **27**, 137 (2006).
[7] R. Bouffanais, M. O. Deville, and E. Leriche, "Large-eddy simulation of the flow in a lid-driven cubical cavity," Phys. Fluids **19**, 055108 (2007).
[8] R. Bouffanais and D. Lo Jacono, "Transitional cylindrical swirling flow in presence of a flat free surface," Comput. Fluids **38**, 1651 (2009).
[9] M. Brøns, W. Z. Shen, J. N. Sørensen, and W. J. Zhu, "The influence of imperfections on the flow structure of steady vortex breakdown bubbles," J. Fluid Mech. **578**, 453 (2007).
[10] M. Brøns, M. C. Thompson, and K. Hourigan, "Dye visualization near a three-dimensional stagnation point: Application to the vortex breakdown bubble," J. Fluid Mech. **622**, 177 (2009).
[11] M. Brøns, L. K. Voigt, and J. N. Sørensen, "Streamline topology of steady axisymmetric vortex breakdown in a cylinder with co- and counter-rotating end-covers," J. Fluid Mech. **401**, 275 (1999).
[12] M. Brøns, L. K. Voigt, and J. N. Sørensen, "Topology of vortex breakdown bubbles in a cylinder with a rotating bottom and a free surface," J. Fluid Mech. **428**, 133 (2001).
[13] C. Day, J. A. Harris, J. Soria, D. G. Boger, and M. C. Welsh, "Behavior of an elastic fluid in cylindrical swirling flow," Exp. Therm. Fluid Sci. **12**, 250 (1996).
[14] J. Donea, A. Huerta, J.-Ph. Ponthot, and A. Rodriguez-Ferran, *Arbitrary Lagrangian–Eulerian Methods*, Encyclopedia of Computational Mechanics, edited by E. Stein, R. de Borst, and T. J. R. Hugues (Wiley, New York, 2004), Vol. 1, Chap. 14.
[15] M. P. Escudier, "Observations of the flow produced in a cylindrical container by a rotating endwall," Exp. Fluids **2**, 189 (1984).
[16] M. P. Escudier and L. M. Cullen, "Flow of a shear-thinning liquid in a cylindrical container with a rotating end wall," Exp. Therm. Fluid Sci. **12**, 381 (1996).
[17] M. P. Escudier and J. J. Keller, "Recirculation in swirling flow—A manifestation of vortex breakdown," AIAA J. **23**, 111 (1985).
[18] J. H. Faler and S. Leibovich, "Disrupted states of vortex flow and vortex breakdown," Phys. Fluids **20**, 1385 (1977).
[19] M. G. Hall, "Vortex breakdown," Annu. Rev. Fluid Mech. **4**, 195 (1972).
[20] A. H. Hirsa, J. M. Lopez, and R. Miraghaie, "Symmetry breaking to a rotating wave in a lid-driven cylinder with a free surface: Experimental observation," Phys. Fluids **14**, L29 (2002).
[21] K. Hourigan, L. J. W. Graham, and M. C. Thompson, "Spiral streaklines in pre-vortex breakdown regions of axisymmetrical swirling flows," Phys. Fluids **7**, 3126 (1995).
[22] R. Iwatsu, "Analysis of flows in a cylindrical container with rotating bottom and top undeformable free surface," JSME Int. J., Ser. B **47**, 549 (2004).
[23] R. Iwatsu, "Numerical study of flows in a cylindrical container with rotating bottom and top flat free surface," J. Phys. Soc. Jpn. **74**, 333 (2005).
[24] G. E. Karniadakis, M. Israeli, and S. A. Orszag, "High-order splitting methods for the incompressible Navier–Stokes equations," J. Comput. Phys. **97**, 414 (1991).
[25] R. R. Kerswell, "Elliptical instability," Annu. Rev. Fluid Mech. **34**, 83 (2002).
[26] J. R. Koseff and R. L. Street, "The lid-driven cavity flow: A synthesis of qualitative and quantitative observations," J. Fluids Eng. **106**, 390 (1984).
[27] J. R. Koseff and R. L. Street, "Visualization studies of a shear driven 3-dimensional recirculating flow," J. Fluids Eng. **106**, 21 (1984).
[28] S. Leibovich, "Structure of vortex breakdown," Annu. Rev. Fluid Mech. **10**, 221 (1978).
[29] D. Lo Jacono, J. N. Sørensen, M. C. Thompson, and K. Hourigan, "Control of vortex breakdown in a closed cylinder with a small rotating rod," J. Fluids Struct. **24**, 1278 (2008).
[30] J. M. Lopez, "Unsteady swirling flow in an enclosed cylinder with reflectional symmetry," Phys. Fluids **7**, 2700 (1995).
[31] J. M. Lopez, F. Marques, A. H. Hirsa, and R. Miraghaie, "Symmetry breaking in free-surface cylinder flows," J. Fluid Mech. **502**, 99 (2004).
[32] Y. Maday and A. T. Patera, *State-of-the-Art Survey on Computational Mechanics*, edited by A. K. Noor and J. T. Oden (ASME, New York, 1989), pp. 71–142.
[33] D. L. Marcus and S. A. Berger, "The interaction between a counter-rotating vortex pair in vertical ascent and a free surface," Phys. Fluids A **1**, 1988 (1989).
[34] R. Miraghaie, J. M. Lopez, and A. H. Hirsa, "Flow induced patterning at the air-water interface," Phys. Fluids **15**, L45 (2003).
[35] T. Mullin, J. J. Kobine, S. J. Tavener, and K. A. Cliffe, "On the creation of stagnation points near straight and sloped walls," Phys. Fluids **12**, 425 (2000).
[36] L. Mununga, K. Hourigan, M. C. Thompson, and T. Leweke, "Confined flow vortex breakdown control using a small rotating disk," Phys. Fluids **16**, 4750 (2004).
[37] V. L. Okulov, J. N. Sørensen, and L. K. Voigt, "Vortex scenario and bubble generation in a cylindrical cavity with rotating top and bottom," Eur. J. Mech. B/Fluids **24**, 137 (2005).
[38] J. C. F. Pereira and J. M. M. Sousa, "Confined vortex breakdown generated by a rotating cone," J. Fluid Mech. **385**, 287 (1999).
[39] M. Piva and E. Meiburg, "Steady axisymmetric flow in an open cylindrical container with a partially rotating bottom wall," Phys. Fluids **17**, 063603 (2005).
[40] C. Pozrikidis, *Introduction to Theoretical and Computational Fluid Dynamics* (Oxford University Press, New York, 1997), Chap. 3, pp. 135–138.
[41] R. Ronnenberg, "Ein selbstjustierendes 3-Komponenten-Laserdoppleranemometer nach dem Vergeichsstrahlvefahren, angewandt auf Untersuchungen in einer stationären zylinder-symmetrischen Drehströmung mit einen Rückströmgebiet," Max-Planck-Institut für Strömungsforschung, Göttingen Technical Report No. 19, 1977.
[42] T. Sarpkaya, "Vorticity, free surface, and surfactants," Annu. Rev. Fluid Mech. **28**, 83 (1996).
[43] V. Shtern and F. Hussain, "Collapse, symmetry breaking, and hysteresis in swirling flows," Annu. Rev. Fluid Mech. **31**, 537 (1999).
[44] J. N. Sørensen, "Visualization of rotating fluid flow in a closed cylinder," Department of Fluid Mechanics, Technical University of Denmark Technical Report No. AFM 92-06, 1992.
[45] F. Sotiropoulos and Y. Ventikos, "Transition from bubble-type vortex breakdown to columnar vortex in a confined swirling flow," Int. J. Heat Fluid Flow **19**, 446 (1998).
[46] F. Sotiropoulos and Y. Ventikos, "The three-dimensional structure of confined swirling flows with vortex breakdown," J. Fluid Mech. **426**, 155 (2001).
[47] A. Spohn, M. Mory, and E. J. Hopfinger, "Observations of vortex breakdown in an open cylindrical container with a rotating bottom," Exp. Fluids **14**, 70 (1993).
[48] A. Spohn, M. Mory, and E. J. Hopfinger, "Experiments on vortex breakdown in a confined flow generated by a rotating disc," J. Fluid Mech. **370**, 73 (1998).
[49] J. R. Stokes, L. J. W. Graham, N. J. Lawson, and D. V. Boger, "Swirling flow of viscoelastic fluids. Part 1. Interaction between inertia and elasticity," J. Fluid Mech. **429**, 67 (2001).
[50] J. R. Stokes, L. J. W. Graham, N. J. Lawson, and D. V. Boger, "Swirling flow of viscoelastic fluids. Part 2. Elastic effects," J. Fluid Mech. **429**, 117 (2001).
[51] D. T. Valentine and C. C. Jahnke, "Flows induced in a cylinder with both end walls rotating," Phys. Fluids **6**, 2702 (1994).
[52] H. U. Vogel, "Experimentelle Ergebnisse über die laminare Strömung in einem zylindrischen Gehäuse mit darin rotierender scheibe," Max-Planck-Institut für Strömungsforschung Report No. 6, 1968.
[53] S. C. Xue, N. Phan-Thien, and R. I. Tanner, "Fully three-dimensional, time-dependent numerical simulations of Newtonian and viscoelastic swirling flows in a confined cylinder—Part I. Method and steady flows," J. Non-Newtonian Fluid Mech. **87**, 337 (1999).
[54] D. L. Young, H. J. Sheen, and T. Y. Hwu, "Period-doubling route to chaos for a swirling flow in an open cylindrical container with a rotating disk," Exp. Fluids **18**, 389 (1995).